Available online at www.sciencedirect.com
SCIENCE DIRECT®
Optics Communications 259 (2006) 19–31
OPTICS COMMUNICATIONS
www.elsevier.com/locate/optcom

Combined analyser-based and propagation-based phase-contrast imaging of weak objects

Ya.I. Nesterets [a,*], T.E. Gureyev [a], K.M. Pavlov [b,c], D.M. Paganin [a,b,c], S.W. Wilkins [a]

[a] CSIRO Manufacturing and Infrastructure Technology, Private Bag 33, Clayton South, Vic. 3169, Australia
[b] School of Physics, Monash University, Vic. 3800, Australia
[c] Monash Centre for Synchrotron Science, Monash University, Vic. 3800, Australia

Received 30 May 2005; received in revised form 27 July 2005; accepted 26 August 2005

Abstract

A new theoretical method combining analyser-based and propagation-based hard X-ray phase-contrast imaging is investigated. Unlike the previous theoretical model of the combined imaging method constructed under the assumption of slow variation of the individual transfer functions (large Fresnel numbers), a new model proposed in this paper uses the assumption of a weak scatterer (analogous to the first Born approximation). Consequently, the results are not limited to the case of short propagation distances or low-resolution imaging. An explicit expression for the combined transfer function is derived and analytical and numerical examples solving related inverse imaging problems are presented.

PACS: 07.85.−m; 42.25.Fx; 42.25.Kb; 42.30.Lr; 42.30.Rx; 42.30.Va; 42.30.Wb

Keywords: X-ray instruments; Diffraction; Coherence; Optical transfer functions; Phase retrieval; Image forming and reconstruction

1. Introduction

Hard X-ray phase-contrast imaging is a powerful tool for imaging the internal structure of thick optically opaque objects [1]. Due to the penetrating power of high-energy X-ray radiation it is possible to image many types of biological and other samples in their native state without sectioning or staining. Full three-dimensional imaging can be performed in this modality with the help of computed tomography [2–8]. Compared to conventional absorption imaging, phase-contrast imaging can often produce much clearer images of samples consisting predominantly of light chemical elements (e.g., biological samples) [1]. The improved contrast is achieved because at high X-ray energies the real part of the refractive index decrement (which is responsible for phase contrast) of such samples is several orders of magnitude larger than its imaginary part (which determines absorption contrast).

Two modes of hard X-ray phase contrast imaging, namely propagation-based imaging (PBI) [9–11] and analyser-crystal based imaging (ABI) [12–15], have become particularly popular using both synchrotron radiation and laboratory X-ray sources. In PBI phase contrast is formed as a result of free-space propagation of an X-ray beam transmitted through a sample. The detector is placed at a sufficient distance from the sample to allow the transformation of transverse phase-shift variations (induced by the transmission of the incident beam through the sample) into intensity variations by means of Fresnel diffraction. In ABI, the transformation of the phase shifts into intensity variations in the detector plane is achieved by allowing the transmitted beam to be diffracted by a near-perfect analyser crystal which plays the role of a one-dimensional Fourier filter [16]. The two imaging methods have their relative advantages and disadvantages. In particular, PBI is simpler to implement and is sensitive to phase variations in any

* Corresponding author. Tel.: +61 3 9545 2916; fax: +61 3 9544 1128.
E-mail address: Yakov.Nesterets@csiro.au (Ya.I. Nesterets).

0030-4018/$ - see front matter © 2005 Elsevier B.V. All rights reserved.
doi:10.1016/j.optcom.2005.08.055

direction orthogonal to the optical axis, while ABI can produce stronger image contrast and better scatter rejection but is sensitive to phase variations in one direction only. A detailed quantitative comparison of PBI and ABI can be found, for example, in [17].

Recently, it has been shown both theoretically [18] and experimentally [19,20] that PBI and ABI can be merged into a single imaging technique which combines some advantages of the two methods. The theoretical model of the combined PBI/ABI technique can also be used for better understanding and quantitative analysis of certain contrast features in conventional ABI. Such features may appear due to effects of free-space propagation inevitably present in realistic experimental ABI set-ups due to finite distances between the source, the sample and the detector. The combined PBI/ABI optical transfer functions have to be calculated also as a first step for enabling computed tomography utilising this advanced contrast mechanism. The latter problem requires solution of the inverse problem of reconstruction of the object-plane complex amplitude from one or more images collected at one or more sample-to-detector distances, angular positions or transverse orientations of the analyser crystal and/or different energies of the incident X-ray radiation. The well-known phase-retrieval problem [21] can be viewed as a part of this more general inverse problem.

The combined PBI/ABI contrast transfer functions have been previously calculated and solutions to some practical inverse problems have been obtained under the assumptions of slow variation of the separate PBI and ABI transfer functions [18]. This assumption was shown to be equivalent to the requirement for both the Fresnel and the Takagi numbers [18] to be much larger than unity. This condition allows one to linearize the corresponding diffraction integrals with respect to the phase, and thus obtain explicit analytical solutions to the direct and inverse imaging problems. Another well-known case where the diffraction integrals can be linearized is that of a "weak scatterer", which is used in particular to derive the first Born approximation in a variety of scattering problems [22–24]. Results obtained under this latter assumption are usually complementary to those that can be derived using the condition of slow variation of transfer functions [25]. In particular, while the "slow variation" condition usually limits the applicability of the corresponding results to the cases of short propagation distances or low resolution imaging [18], the "weak scatterer" condition does not impose any limitations on the propagation distances or spatial resolution of images as long as both the absorption and phase shifts introduced by the object into the transmitted beam are sufficiently small. Under these assumptions it is often possible to analyse the dependence of image contrast on such factors as radiation wavelength, geometrical parameters of the imaging layout, etc. [23]. In this paper we will derive the linearized combined PBI/ABI transfer function under the "weak scatterer" assumption and show both theoretically and by numerical examples how certain direct and inverse imaging problems can be solved using the obtained formalism.

2. General formalism

We restrict our consideration to the case of a two-dimensional linear shift-invariant (LSI) optical system, i.e., a system whose response to an arbitrary input wave $E_{\text{in}}(x,y)$ is described completely by a point-spread function (PSF) $G(x,y)$. The output wave $E_{\text{out}}(x,y)$ is therefore a convolution of the input wave and the PSF,

$$E_{\text{out}}(x,y) = G \otimes E_{\text{in}} \equiv \int\int \mathrm{d}x'\,\mathrm{d}y' G(x',y') E_{\text{in}}(x-x',y-y'), \tag{1}$$

where the symbol $\otimes$ denotes convolution.

In the following, we represent the amplitude of the input wave as $E_{\text{in}}(x,y) = \exp(-\mu(x,y) + \mathrm{i}\varphi(x,y))$, where we have introduced the real attenuation function μ and phase shift φ. It is convenient to decompose both μ and φ into their mean values and deviations from the means, i.e., $\mu(x,y) = \bar{\mu} + \Delta\mu(x,y)$ and $\varphi(x,y) = \bar{\varphi} + \Delta\varphi(x,y)$.

2.1. Weak object approximation

Let us assume that both functions, $\Delta\mu(x,y)$ and $\Delta\varphi(x,y)$, in the input wave are small compared to unity. Then the amplitude of the input wave can be represented in the following form:

$$E_{\text{in}}(x,y) \cong \bar{E}_{\text{in}}(1 + \Delta E_{\text{in}}(x,y)), \tag{2}$$

where $\bar{E}_{\text{in}} \equiv \exp(-\bar{\mu} + \mathrm{i}\,\bar{\varphi})$ and $\Delta E_{\text{in}}(x,y) \equiv -\Delta\mu(x,y) + \mathrm{i}\Delta\varphi(x,y)$.

Assuming that Eq. (2) is valid, Eq. (1) takes the following form:

$$E_{\text{out}}(x,y) \cong \bar{E}_{\text{in}}\{t + G \otimes \Delta E_{\text{in}}\}, \tag{3}$$

where $t \equiv \int\int \mathrm{d}x\,\mathrm{d}y G(x,y) = [G](0,0)$ is the system amplitude transmittance coefficient (ATC), and hereafter the square brackets designate the Fourier transform. The corresponding intensity of the output wave is approximately expressed as

$$I_{\text{out}}(x,y) \cong \bar{I}_{\text{in}}\{T + 2Re(\tilde{G} \otimes \Delta E_{\text{in}})\}, \tag{4}$$

where $\bar{I}_{\text{in}} \equiv |\bar{E}_{\text{in}}|^2 = \exp(-2\bar{\mu})$, $T = |t|^2$ is the system transmittance, $\tilde{G} = t^* G$ (superscript asterisk denotes the complex conjugate) and we have neglected the term quadratic with respect to ΔE_{in}. The Fourier transform of the intensity is then written as follows:

$$[I_{\text{out}}](u,v) \cong \bar{I}_{\text{in}}\{T\delta(u)\delta(v) - 2([\tilde{G}^{\text{r}}][\Delta\mu] + [\tilde{G}^{\text{i}}][\Delta\varphi])\}, \tag{5}$$

where $\delta(u)$ is the Dirac delta-function, superscript indices 'r' and 'i' denote the real and imaginary part, respectively, and Eq. (5) holds for all points (u,v) in the reciprocal space. In the following we will refer to $[\tilde{G}^{\text{r}}](u,v)$ and $[\tilde{G}^{\text{i}}](u,v)$ as the amplitude transfer function (ATF) and phase transfer function (PTF), respectively.

It is of practical interest to consider the case when the LSI system consists of two cascaded LSI sub-systems. This complex system describes a typical situation when a wave is transmitted through two consecutive LSI optical systems. Then the PSF G of the system is represented as a convolution of the sub-systems' PSFs G_1 and G_2, so that $G = G_1 \otimes G_2$. As can be shown, the ATC t of the system is simply a product of the sub-systems' ATCs, $t = t_1 t_2$, and the corresponding ATF and PTF of the system relate to those of the sub-systems as follows:

$$\begin{aligned}[\tilde{G}^{\mathrm{r}}] &= [\tilde{G}_1^{\mathrm{r}}][\tilde{G}_2^{\mathrm{r}}] - [\tilde{G}_1^{\mathrm{i}}][\tilde{G}_2^{\mathrm{i}}],\\ [\tilde{G}^{\mathrm{i}}] &= [\tilde{G}_1^{\mathrm{r}}][\tilde{G}_2^{\mathrm{i}}] + [\tilde{G}_1^{\mathrm{i}}][\tilde{G}_2^{\mathrm{r}}].\end{aligned} \tag{6}$$

It is worth mentioning one important consequence (corollary) of the above expressions. To obtain this, we reorder terms in Eq. (5) as follows:

$$\begin{aligned}&[\tilde{G}^{\mathrm{r}}][\Delta\mu] + [\tilde{G}^{\mathrm{i}}][\Delta\varphi]\\ &\quad = \{[\tilde{G}_1^{\mathrm{r}}][\Delta\mu] + [\tilde{G}_1^{\mathrm{i}}][\Delta\varphi]\}[\tilde{G}_2^{\mathrm{r}}] + \{[\tilde{G}_1^{\mathrm{r}}][\Delta\varphi] - [\tilde{G}_1^{\mathrm{i}}][\Delta\mu]\}[\tilde{G}_2^{\mathrm{i}}].\end{aligned} \tag{7}$$

This equation shows that various direct and inverse imaging algorithms designed for special categories of sample, such as e.g., pure phase (non-absorbing) or homogeneous (consisting of a single material) samples [26], cannot be simply used in a sequential manner in order to solve the corresponding problems for the combined system. This is because, as Eq. (7) shows, the phase and absorption effects are "mixed" at the first stage (by the first sub-system), so the simplified models of the sample are no longer applicable at the entrance into the second sub-system.

2.2. PBI, ABI and combined ABI/PBI transfer functions

It is well known that free-space propagation and X-ray diffraction in a perfect flat crystal present two examples of LSI systems. The explicit expressions for the ATF and PTF, corresponding to PBI (in the paraxial approximation) and ABI, are as follows [23,24]:

$$\begin{aligned}[\tilde{G}^{\mathrm{r}}_{\mathrm{PBI}}](u,v;z_u,z_v) &= \cos(\pi\lambda(z_u u^2 + z_v v^2)),\\ [\tilde{G}^{\mathrm{i}}_{\mathrm{PBI}}](u,v;z_u,z_v) &= \sin(\pi\lambda(z_u u^2 + z_v v^2)),\end{aligned} \tag{8}$$

$$\begin{aligned}[\tilde{G}^{\mathrm{r}}_{\mathrm{ABI}}](u;\omega) &= (1/2)\{r(\omega+\lambda u)r^*(\omega) + r^*(\omega-\lambda u)r(\omega)\},\\ [\tilde{G}^{\mathrm{i}}_{\mathrm{ABI}}](u;\omega) &= (\mathrm{i}/2)\{-r(\omega+\lambda u)r^*(\omega) + r^*(\omega-\lambda u)\, r(\omega)\},\end{aligned} \tag{9}$$

where z_u and z_v are the effective propagation distances for transverse modulations in the x and y directions, respectively (see Fig. 1 for the axis directions). In Eq. (9) $r(\omega)$ denotes the amplitude reflectance or transmittance coefficient of the crystal (either in Bragg or Laue geometry) as a function of its angular deviation ω from the exact Bragg position. Note that transfer functions of the analyser crystal in Eq. (9) depend only on u, the coordinate dual to x.

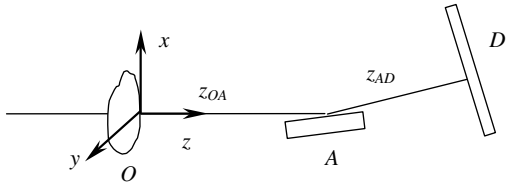

Fig. 1. Phase-contrast imaging setup used in the numerical simulations in the case of a plane monochromatic incident wave.

Thus, we implicitly assumed that the plane of diffraction of the analyser coincides with the plane x–z.

We highlight one important feature of the imaging set-up, combining both propagation and analyser-based phase contrast. If the diffracted wave is used for image formation, then, for an asymmetrical reflection, the change of spatial frequencies u should be taken into account for any free space propagation after the crystal. This is due to the fact that for an asymmetrical reflection the width of the reflected beam is equal to that of the incident beam divided by b, where $b \equiv \gamma_0/|\gamma_h|$ is the asymmetry factor of the crystal and γ_0 and γ_h are the directional cosines of the incident and reflected beam, respectively. Asymmetry of the analyser crystal can be easily taken into account by appropriate choice of the effective propagation distances z_u and z_v in Eq. (8). Designating by z_{OA} and z_{AD} the object-to-analyser and analyser-to-detector distances, respectively (see also Fig. 1), we can write the corresponding transfer functions in Eq. (6) as follows:

$$\begin{aligned}[\tilde{G}_1^{\mathrm{r}}](u,v) &= [\tilde{G}^{\mathrm{r}}_{\mathrm{PBI}}](u,v;b^{-2}z_{\mathrm{OA}} + z_{\mathrm{AD}}, z_{\mathrm{OA}} + z_{\mathrm{AD}}),\\ [\tilde{G}_1^{\mathrm{i}}](u,v) &= [\tilde{G}^{\mathrm{i}}_{\mathrm{PBI}}](u,v;b^{-2}z_{\mathrm{OA}} + z_{\mathrm{AD}}, z_{\mathrm{OA}} + z_{\mathrm{AD}}),\\ [\tilde{G}_2^{\mathrm{r}}](u,v) &= [\tilde{G}^{\mathrm{r}}_{\mathrm{ABI}}](b^{-1}u;\omega),\\ [\tilde{G}_2^{\mathrm{i}}](u,v) &= [\tilde{G}^{\mathrm{i}}_{\mathrm{ABI}}](b^{-1}u;\omega).\end{aligned} \tag{10}$$

We should emphasize that spatial frequencies u and v in Eq. (10) correspond to the output (image) plane of the optical system.

Below we perform a quantitative analysis of the combined transfer functions calculated according to Eqs. (7)–(10), in the context of both forward and inverse problems. The moduli of the combined transfer functions, together with those of the ABI transfer functions, are presented versus spatial frequency u in Fig. 2, for different values of the deviation angle ω of the analyser. The following parameters were used for numerical calculations: plane incident wave of energy 20 keV, symmetrical (1 1 1)-reflection of the silicon analyser crystal, 2 m object-to-detector free-space propagation distance. As follows from Figs. 2(a) and (b), for the analyser crystal set into the exact Bragg position the phase transfer function of the crystal is very small. As a result, the combined transfer functions are simply the corresponding transfer functions for free space propagation modulated by the amplitude transfer function of the analyser which acts as a low frequency filter in this case. For nonzero analyser deviations, exceeding the half

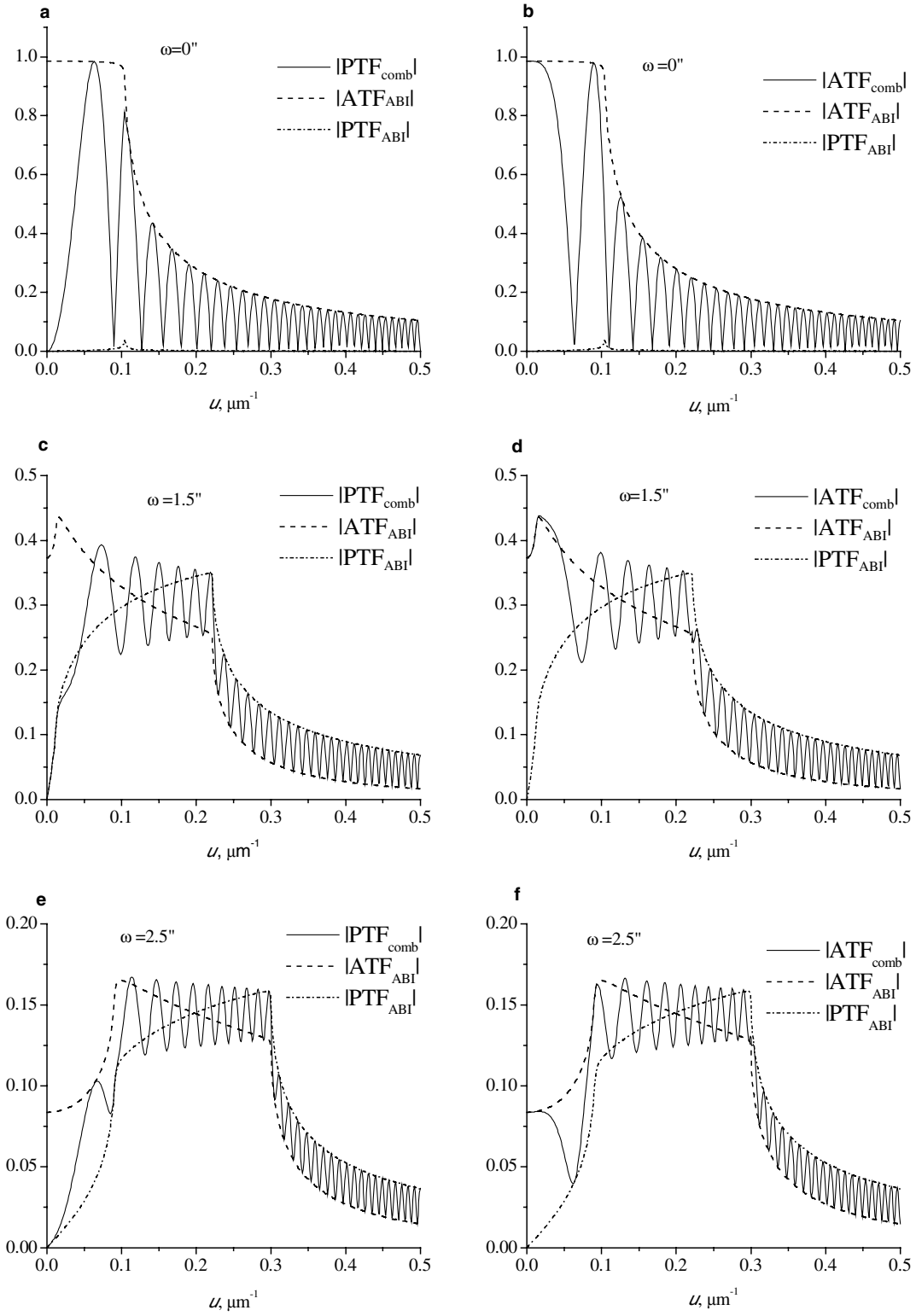

Fig. 2. Moduli of the combined phase (a, c, e) and amplitude (b, d, f) transfer functions (solid lines), together with those of the ABI amplitude (dashed lines) and phase (dotted-dashed lines) transfer functions, for different values of the deviation angle ω of the analyser crystal: $\omega = 0''$ (a, b), $\omega = 1.5''$ (c, d) and $\omega = 2.5''$ (e, f). Plane monochromatic incident X-ray waves of 20 keV energy, symmetrical (1 1 1)-reflection of silicon analyser crystal and 2 m object-to-detector distance were used in numerical calculations.

width at half maximum of the crystal rocking curve (1.35″ for symmetrical Si(1 1 1)-reflection of the σ-polarised X-rays at 20 keV), the crystal's phase and amplitude transfer functions are of the same order of magnitude, and the combined transfer functions have more complex forms (see Figs. 2(c)–(f)). We should underline that unlike the

pure propagation transfer functions the combined transfer functions have no zeroes except for a zero of the PTF at $u = 0$. Figs. 2(c)–(f) indicate that there is no loss of information in the process of combined PB/AB imaging and thus the inverse problem of amplitude/phase reconstruction can be solved potentially with high accuracy. The zero value of the combined PTF at $u = 0$ indicates that information about the mean phase shift is irretrievably lost in the process of imaging and cannot be retrieved from the image without additional information (for example, a priori knowledge of the relationship between phase and amplitude of the incident wave). It is also remarkable that the maximum values of the combined transfer functions decrease with the analyser deviation as the reflectivity of the thick (semi-infinite) crystal monotonically decreases with the deviation angle.

2.3. Remark

It was recently rediscovered [27] that Eq. (5) is valid in PBI if a less stringent condition on the phase shift function, due to Guigay [28], is fulfilled: $|\varphi(x,y) - \varphi(x - \lambda z u, y - \lambda z v)| \ll 1$ for all points (x,y) and (u,v) (see also [29]). Similarly, in order that Eq. (5) be valid in the case of ABI, the characteristic length scale of phase variations in the input wave, along the surface of the analyser crystal, should be much larger than the extinction length l_{ext} of the analyser crystal (e.g., $l_{\text{ext}} = 15.4$ μm for symmetrical Si(1 1 1)-reflection of σ-polarised X-rays at 20 keV). Thus our analysis given above, in Section 2.1, is applicable not only to true weak objects but also to *weakly absorbing objects with slowly varying refractive index and projected thickness*.

3. Numerical results and discussion

Here, we apply results of the previous section to the solution of forward and inverse problems in combined PBI/ABI phase-contrast imaging, for two model objects. Let such an object be illuminated by a plane monochromatic wave, $\exp(\mathrm{i}kz)$, with $q(x,y) = \exp(-\mu(x,y) + \mathrm{i}\varphi(x,y))$ being the object transmission function. The corresponding imaging setup is schematically presented in Fig. 1 and consists of a test object (O), analyser crystal (A) and detector (D). In order to satisfy Eq. (5), the object attenuation function and phase have to satisfy conditions formulated in the previous section, i.e., (1) deviations of the attenuation $\mu(x,y)$ function from its mean value should be small compared to unity, and (2) variations of the phase $\varphi(x,y)$ should be small on the length scale $\lambda z u$ for PBI and of the order of several extinction lengths for ABI.

3.1. Hybrid method: numerical simulations

Below we present the results of numerical simulations of the phase-contrast imaging (forward problem) for two homogeneous objects (for such homogeneous objects one has $\frac{\mu(x,y)}{\varphi(x,y)} = -\frac{\beta}{\delta} = \text{constant}$ [26], where δ and β are the real and imaginary parts of the difference between the refractive index n_1 of the material from which the object is composed and the refractive index n_2 of the material of the surrounding medium of constant thickness for all points (x,y), i.e., $n_1 - n_2 = -\delta + \mathrm{i}\beta$).

Object 1: two 3 mm diameter crossed polyethylene cylinders in water (2048×2048 pixels, 4.39 μm pixel size), $\varphi_{\max} = 9.129$ rad, $\mu_{\max} = -0.05471$, $\delta/\beta = 166.9$.

Object 2: two 3 mm diameter crossed Perspex cylinders in water (2048×2048 pixels, 4.39 μm pixel size), $\varphi_{\max} = -25.617$ rad, $\mu_{\max} = -0.0189$, $\delta/\beta = -1355$.

The complex transmission function of the homogeneous object is expressed as follows:

$$q(x,y) = \exp(\varphi(x,y)(\mathrm{i} + \beta/\delta)). \tag{11}$$

The reason for the above choice of test objects can be clarified by analysing Table 1. The first three rows present the values of linear phase shift and linear absorption coefficient for polyethylene, Perspex and water (all are relative to vacuum). Note the large values of the phase shift in the case of the polyethylene and Perspex in vacuum. For example, a 3 mm diameter polyethylene cylinder in vacuum causes a maximum phase shift of −166 rad which is more than 10 times larger than that for the same cylinder in water. Our calculations showed (see also Section 3.3) that the maximum values of $|\varphi(x) - \varphi(x - \lambda z u)|$ and $|\varphi(x) - \varphi(x - l_{\text{ext}}\gamma_0)|$ are about 6.6 and 7.5 rad, respectively. These values strongly violate the conditions $|\varphi(x) - \varphi(x - \lambda z u)| \ll 1$ and $|\varphi(x) - \varphi(x - l_{\text{ext}}\gamma_0)| \ll 1$ (see Section 2.3) for validity of Eq. (5) in the case of PBI and ABI, respectively. On the other hand, for polyethylene and Perspex placed in water rather than in vacuum, the relative phase shift decreases significantly (see last two rows in Table 1) so that conditions for validity of Eq. (5) can be satisfied (see discussion below, in Section 3.3).

Figs. 3 and 5 present, respectively, simulated images of polyethylene and Perspex cylinders in water, obtained using our hybrid method of propagation-based and analyser-based phase contrast imaging. The following parameters were used in the numerical simulations: X-ray wavelength $\lambda = 0.62$ Å (corresponding to 20 keV X-ray

Table 1
Optical constants of various materials used in numerical simulations of images at X-ray energy 20 keV (values in the first three rows are referred to vacuum)

Substance	Linear phase shift (rad/mm)	Linear absorption coeff. (mm^{-1})	δ/β
Polyethylene, $(C_2H_4)_n$	−55.362	0.035625	3108
Perspex, $(C_5O_2H_8)_n$	−66.944	0.0595	2250
Water, H_2O	−58.405	0.0721	1620
Polyethylene in water	3.043	−0.036475	166.9
Perspex in water	−8.539	−0.0126	−1355

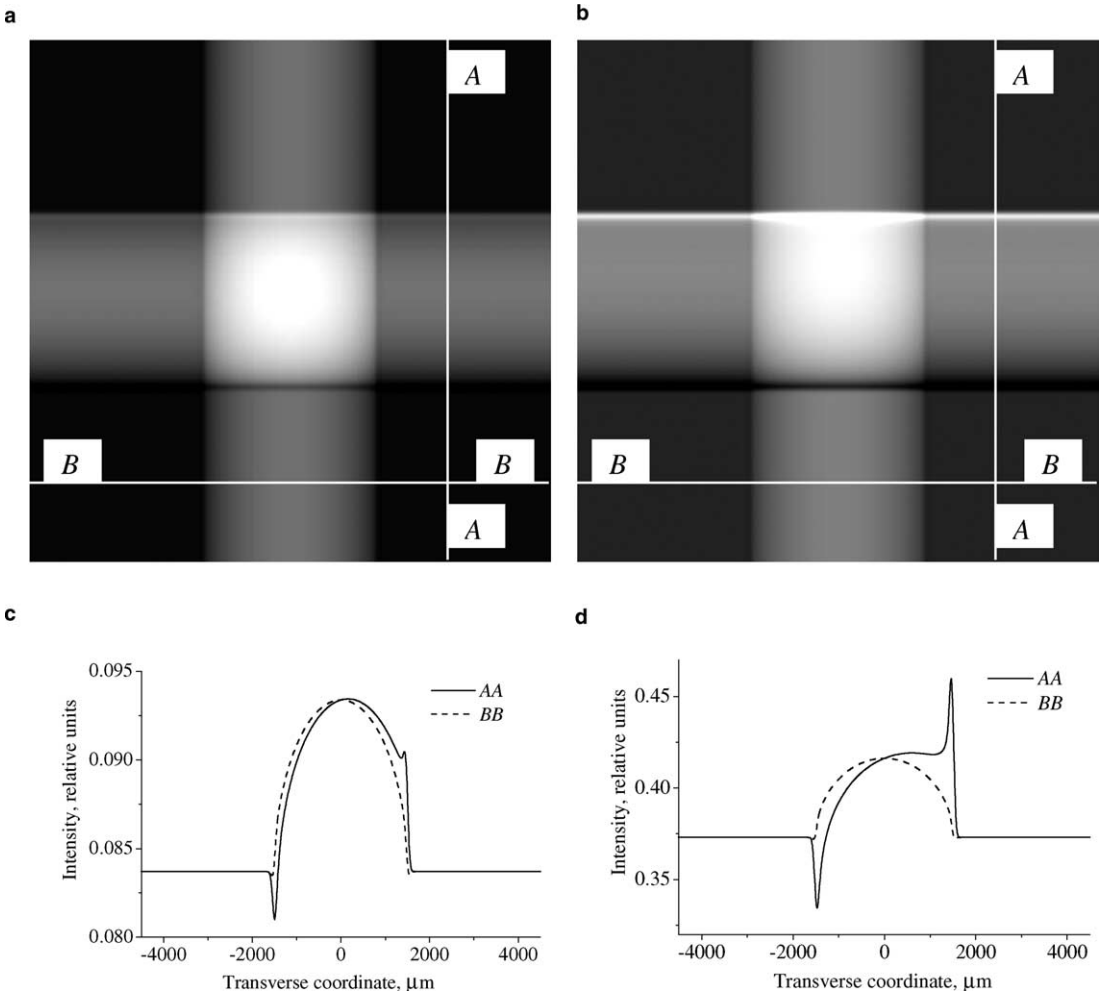

Fig. 3. Calculated images of polyethylene cylinders in water (object 1) at two deviation angles of the analyser crystal: $\omega = 2.5''$ (a) and $\omega = 1.5''$ (b); (c) and (d) – the intensity cross-sections corresponding to the figures (a) and (b). Note that the intensity values are relative to the intensity of the incident plane monochromatic X-ray wave. Plane monochromatic incident X-ray waves of 20 keV energy, symmetrical (1 1 1)-reflection of silicon analyser crystal and 2 m object-to-detector distance were used in numerical calculations.

energy), object-to-image distance $z = 2$ m, symmetrical (1 1 1)-reflection of silicon analyser-crystal with FWHM = $2.7''$ at deviation angles $\omega = 2.5''$ (a) and $1.5''$ (b). In order to simulate a real detector with finite resolution, the calculated images were convolved with a Gaussian PSF whose standard deviation was 10 pixels. Then, if necessary, Poisson noise was generated in the resulting images. We considered three cases: no noise (Figs. 3 and 5), 1% and 10% Poisson noise (see also Table 2). The plane of diffraction was perpendicular to the horizontal cylinder (see also Fig. 1). Figs. 3(c),(d) and 5(c),(d) show intensity cross-sections through the horizontal cylinder (AA) and through the vertical cylinder (BB). The cross-sections AA reveal characteristic analyser-based contrast while the cross-sections BB present pure propagation-based contrast. We should note that without account of finite resolution of the detector, Figs. 3 and 5 would look differently. Indeed, there would be typical Fresnel oscillations due to free space propagation as well as interference fringes due to diffraction in the analyser crystal. In Figs. 3 and 5 presented here these oscillations disappeared due to convolution with the PSF of the detector.

3.2. Solution of the inverse problem

We now pass from the forward problem of determining the image of a model object produced by a hybrid imaging system which combines propagation-based and analyser-based phase contrast, to the corresponding inverse problem of determining information regarding a sample from one or more hybrid phase-contrast images. The following formula was used for the reconstruction of the phase shift induced by the homogeneous object, based on a single hybrid phase-contrast image (it follows directly from Eq. (5) and definition of the homogeneous object):

Table 2
Relative errors in the reconstructed phase (first two values for each combination of deviation angle and noise level) and the mean values of the reconstructed phase (third and fourth values for each combination of deviation angle and noise level)

Sample	No noise	1% Poisson noise	10% Poisson noise	Maximum of $\lvert\varphi(x) - \varphi(x - \lambda z u)\rvert$	Maximum of $\lvert\varphi(x) - \varphi(x - l_{ext}\gamma_0)\rvert$
Object 1					
$\omega = 2.5''$, $z = 2$ m	4.22% (4.22%)	4.25% (4.25%)	7.16% (5.89%)	0.365	0.410
$\langle\varphi\rangle = 4.780$	4.780 (4.786)	4.778 (4.786)	4.574 (4.789)		
Object 1					
$\omega = 1.5''$, $z = 2$ m	5.86% (6.27%)	5.87% (6.29%)	6.89% (6.84%)		
	4.809 (4.897)	4.808 (4.897)	4.652 (4.901)		
Object 2					
$\omega = 2.5''$, $z = 2$ m	6.77% (8.54%)	6.78% (8.59%)	12.07% (10.28%)	1.025	1.153
$\langle\varphi\rangle = -13.413$	−13.828 (−14.261)	−13.813 (−14.262)	−12.156 (-14.294)		
Object 2					
$\omega = 1.5''$, $z = 2$ m	36.12% (52.79%)	36.20% (52.80%)	44.00% (53.53%)		
	−9.001 (−20.438)	−8.989 (−20.439)	−7.825 (−20.483)		

Numbers given in brackets correspond to the phase reconstructions based on the simple relation between average intensities of the input and output waves, $\langle I_{in}\rangle = \langle I_{out}\rangle/T$. Numbers given without brackets have been obtained using the phase reconstruction procedure based on Eq. (13). Last two columns present the quantitative assessment of the 'smoothness' of the phase for PBI and ABI, respectively (see Section 2.3 for detail). $l_{ext}\gamma_0 = 1.524$ μm, $\lambda z u_{max} = 1.24$ μm.

$$\varphi = \frac{\beta}{2\delta}\log\bar{I}_{in} + \left[\frac{1}{2}[(I_{out}/\bar{I}_{in}) - T]\left([\tilde{G}^{r}]\frac{\beta}{\delta} - [\tilde{G}^{i}]\right)^{-1}\right]^{-1}, \quad (12)$$

where $[\,]^{-1}$ denotes inverse Fourier transform. Given the reconstructed phase shift function obtained using the above formula, the complex transmission function of the object can be reconstructed by using Eq. (11). Figs.

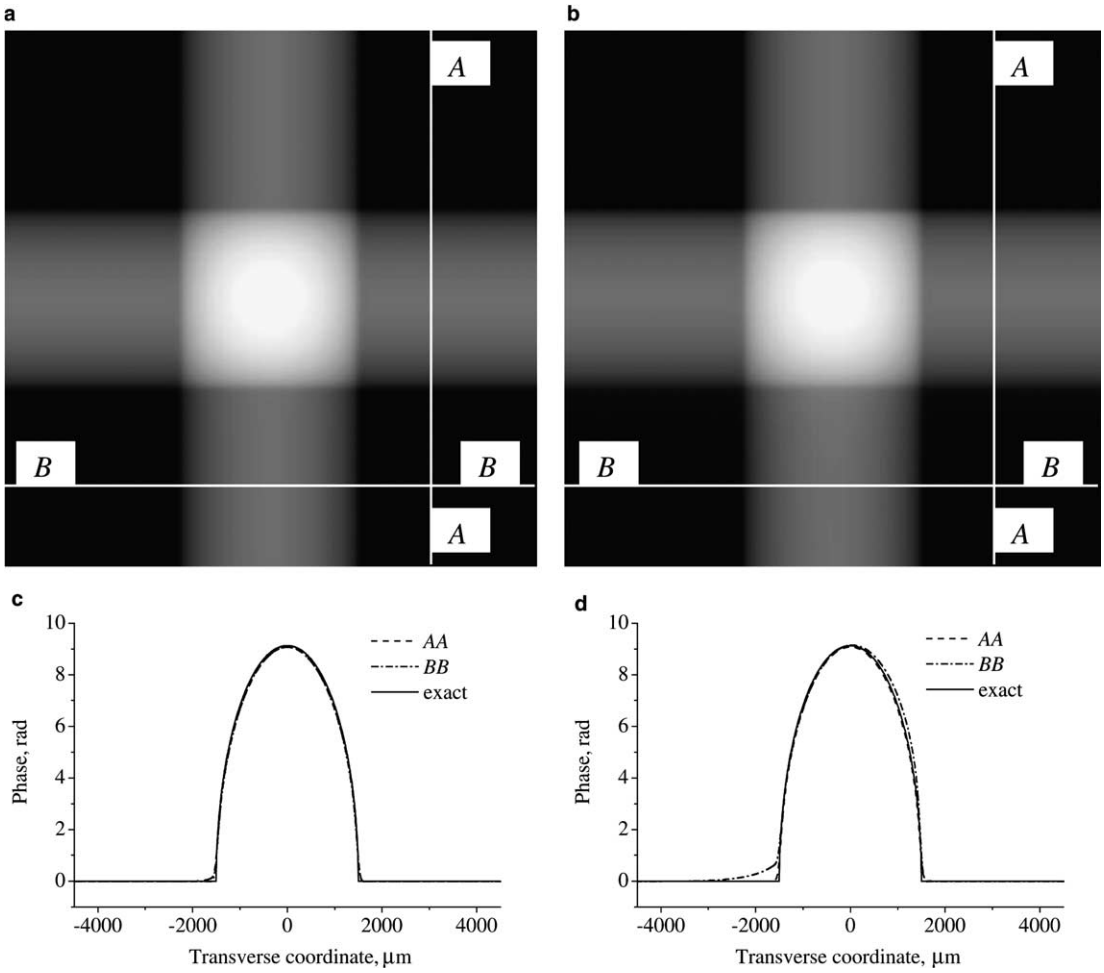

Fig. 4. Reconstructed phase distributions corresponding to Fig. 3.

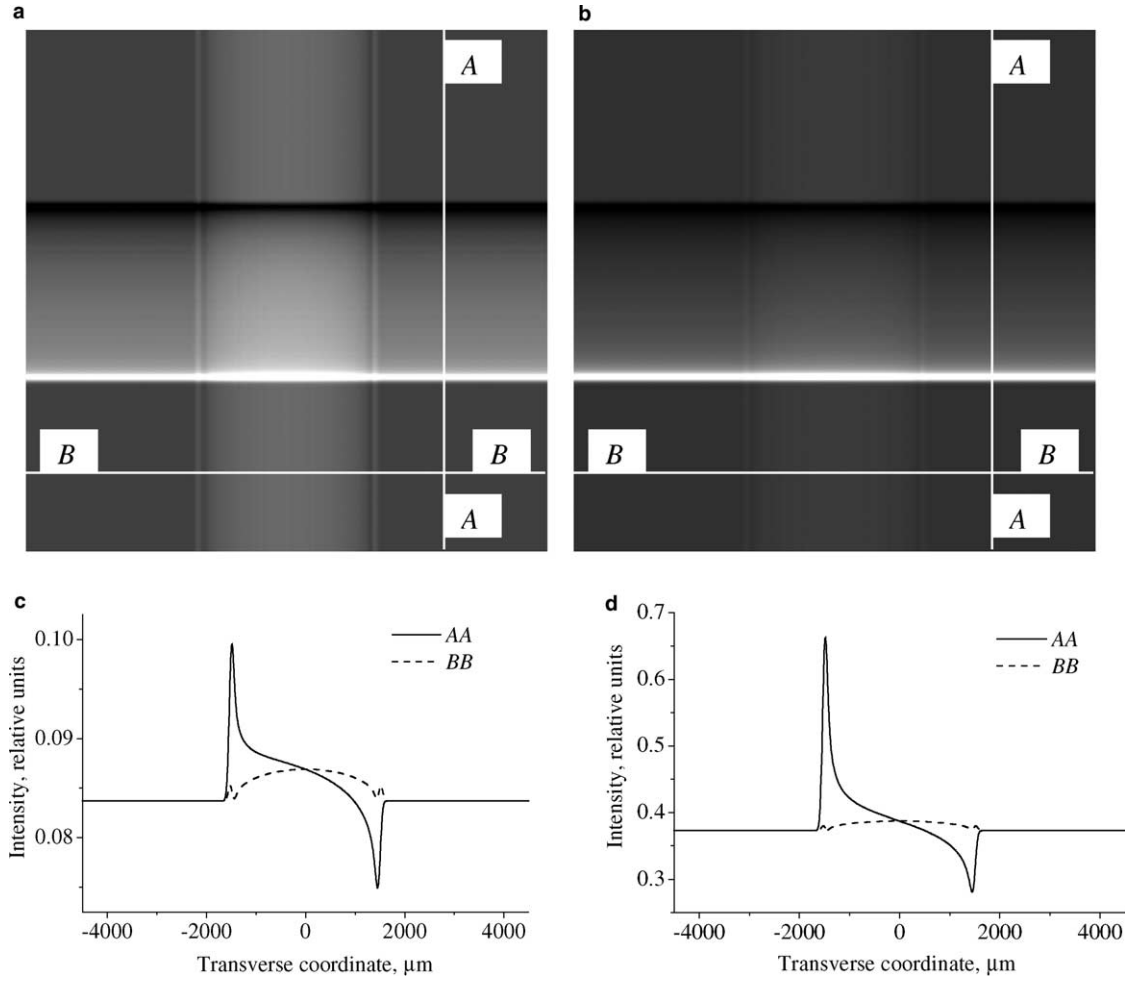

Fig. 5. Calculated images of Perspex cylinders in water (object 2) at two deviation angles of the analyser crystal: $\omega = 2.5''$ (a) and $\omega = 1.5''$ (b); (c) and (d) – the intensity cross-sections corresponding to the figures (a) and (b). The intensity values are relative to the intensity of the incident plane monochromatic X-ray wave. Plane monochromatic incident X-ray waves of 20 keV energy, symmetrical (1 1 1)-reflection of silicon analyser crystal and 2 m object-to-detector distance were used in numerical calculations.

4(a),(b) and 6(a),(b) present reconstructed phase distributions corresponding to Figs. 3(a),(b) and 5(a),(b), respectively. Figs. 4(c),(d) and 6(c),(d) show profiles of the reconstructed phase distributions across the horizontal cylinder (AA) and across the vertical cylinder (BB) together with the exact phase profiles used for image simulations. We should note that Eq. (12) is valid only for homogeneous objects. Reconstruction algorithms for the case of a general object (with independent phase and amplitude spatial modulation of the incident wave) can be found in [24] where the combined transfer functions, Eq. (6), should now be used.

We should note at this stage that parameter $\bar{I}_{\text{in}}$ in Eq. (12), which is related to the mean value of the attenuation function $\bar{\mu}$ via $\bar{I}_{\text{in}} \equiv \exp(-2\bar{\mu})$ (see definitions in Eq. (4)), is not known a priori. It should be calculated from the measured image before applying the phase reconstruction procedure (12). If conditions that have led us to Eq. (2) are satisfied (for example, for a weak object) then $\bar{I}_{\text{in}}$ coincides with the average intensity $\langle I_{\text{in}} \rangle$ of the input wave (see Eq. (2)). According to Eq. (4) the latter is related to the average intensity $\langle I_{\text{out}} \rangle$ of the output wave, via $\langle I_{\text{in}} \rangle = \langle I_{\text{out}} \rangle / T$, where T is the transmittance coefficient of the system. Thus, $\bar{I}_{\text{in}} \approx \langle I_{\text{out}} \rangle / T$. The approximate equality sign underlines that this is true only for weak objects. It was mentioned in Section 2.2 that the resulting Eq. (5) and therefore Eq. (12) is also valid for an incident wave with small transverse intensity variations and slowly varying phase. This means that condition $|\Delta\mu| \ll 1$ is satisfied but the deviations of the phase from its mean value can be large compared to unity. As a result, we still can assume that $\bar{I}_{\text{in}} = \langle I_{\text{in}} \rangle$ but the relationship between $\langle I_{\text{in}} \rangle$ and $\langle I_{\text{out}} \rangle$ is more complex than for a weak object and $\bar{I}_{\text{in}} \neq \langle I_{\text{out}} \rangle / T$. In order to obtain this relationship, we use the following relation between Fourier transforms of the amplitudes of the input and output waves, $[E_{\text{out}}](u,v) = [G](u,v)[E_{\text{in}}](u,v)$, which is the analogue of Eq. (1) written in Fourier space. Using Parseval's theorem we can write

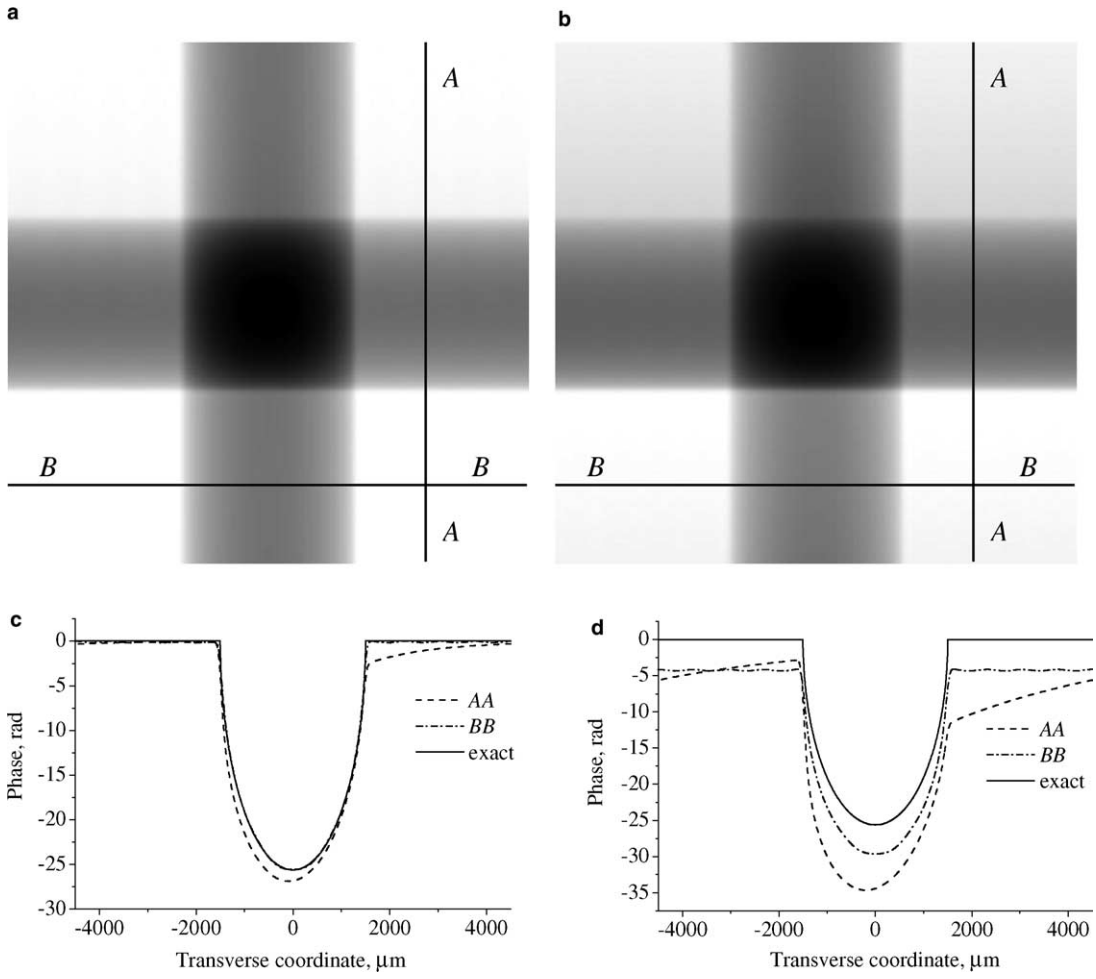

Fig. 6. Reconstructed phase distributions corresponding to Fig. 5.

$$\begin{aligned}
&\int\int \mathrm{d}x\,\mathrm{d}y I_{\mathrm{out}}(x,y)\\
&\quad=\int\int \mathrm{d}u\,\mathrm{d}v|[E_{\mathrm{out}}](u,v)|^2\\
&\quad=\int\int \mathrm{d}u\,\mathrm{d}v|[G](u,v)|^2|[E_{\mathrm{in}}](u,v)|^2\\
&\quad=T\int\int \mathrm{d}u\,\mathrm{d}v|[E_{\mathrm{in}}](u,v)|^2\\
&\qquad+\int\int \mathrm{d}u\,\mathrm{d}v\{|[G](u,v)|^2-T\}\times|[E_{\mathrm{in}}](u,v)|^2\\
&\quad=T\int\int \mathrm{d}x\,\mathrm{d}y I_{\mathrm{in}}(x,y)+\int\int \mathrm{d}u\,\mathrm{d}v\{|[G](u,v)|^2-T\}\\
&\qquad\times|[E_{\mathrm{in}}](u,v)|^2.
\end{aligned}$$

As a result, we have for the integral intensity of the input wave

$$\begin{aligned}
&\int\int \mathrm{d}x\,\mathrm{d}y\; I_{\mathrm{in}}(x,y)\\
&\quad=T^{-1}\int\int \mathrm{d}x\,\mathrm{d}y I_{\mathrm{out}}(x,y)\\
&\qquad-\int\int \mathrm{d}u\,\mathrm{d}v\{|[G](u,v)|^2/T-1\}|[E_{\mathrm{in}}](u,v)|^2. \qquad (13)
\end{aligned}$$

Thus, if the modulus of the imaging system's propagator is not a constant (for example, the propagator of an analyser crystal in contrast to the one for free-space propagation) and the incident wave has a wide range in Fourier space (for example, for a non-weak object), then the second term on the right-hand side of Eq. (13) should be taken into account in order to correctly calculate the average intensity of the incident wave. The evident difficulty of using Eq. (13) is that the integral intensity of the input wave depends not only on the integral intensity of the output (measured) wave but also on the amplitude of the incident wave itself. A possible solution to this problem is that Eqs. (12) and (13) can be used in an iterative manner. First, the average intensity $\bar{I}_{\mathrm{in}}$ of the input wave may be calculated using Eq. (13), neglecting the second term on its right-hand side. This value may then be used for phase reconstruction via Eq. (12), with the reconstructed phase then being used for refinement of the current estimate for $\bar{I}_{\mathrm{in}}$. This process can be continued in an iterative manner until both the reconstructed phase and $\bar{I}_{\mathrm{in}}$ converge.

We performed a reconstruction of the phase of the object transmission function using Eq. (12). In order to

quantitatively characterise the accuracy of the phase reconstruction, errors were calculated according to the following formula:

$$\text{error} = \left[\sum_{i,j} (\varphi_{ij}^{\text{rec}} - \varphi_{ij}^{\text{exact}})^2 \Big/ \sum_{i,j} (\varphi_{ij}^{\text{exact}} - \langle \varphi^{\text{exact}} \rangle)^2 \right]^{1/2}. \quad (14)$$

Table 2 contains the reconstruction errors (first two values for each combination of deviation angle and noise level) as well as the mean values of the reconstructed phase (third and fourth values for each combination of deviation angle and noise level). Numbers given in brackets correspond to the phase reconstructions based on the simple relation between average intensities of the input and output waves, $\langle I_{\text{in}} \rangle = \langle I_{\text{out}} \rangle / T$. Numbers given without brackets have been obtained using the phase reconstruction procedure based on Eq. (13). Analysis of data in Table 2 shows that application of Eq. (13) for calculation of the mean value of intensity of the input wave gives better results for both the reconstruction accuracy and mean phase value in the absence of noise and in the case of the small noise level (second and third columns in Table 2, respectively). However, in the case of the 10% noise level (fourth column) this approach gives a less accurate reconstruction compared to the approach based on the simple relation $\langle I_{\text{in}} \rangle = \langle I_{\text{out}} \rangle / T$. The latter relation gives almost the same value of the mean phase for each deviation angle for all levels of noise presented here. This behaviour can be explained using the following analysis of the influence of noise on the calculation of $\bar{I}_{\text{in}}$ within each of these two methods. In the simplest case, where $\langle I_{\text{in}} \rangle = \langle I_{\text{out}} \rangle / T$, the influence of noise is weak as the average noise value over the whole image is close to zero. In the second approach based on Eq. (13), the mean intensity value of the input wave is calculated not only via the average value of the output wave intensity but also by using the complex amplitude of the input wave. For noise-free images, the reconstructed complex amplitude is free of noise. Noisy images result in noisy reconstructed phase maps and thus noisy reconstructed complex amplitude of the input wave. When the spatial power spectrum of the noise is small compared to that of the true input wave, as will be the case for a small noise level, the influence of noise on the calculation of $\bar{I}_{\text{in}}$ is negligible. However in the case of strong noise the power spectrum of the noise is comparable with that of the true signal and can be even larger for high spatial frequencies (to which $\bar{I}_{\text{in}}$, calculated by using Eq. (13), is usually more sensitive). Thus, large noise strongly affects the calculation of the mean intensity of the input wave and, as a result, the reconstruction accuracy of the phase of the input wave worsens substantially. In order to overcome this difficulty, a low-pass filter could be applied to the reconstructed complex amplitude of the input wave before its use in Eq. (13) for calculation of the mean intensity of the input wave. This step, obviously, needs a priori knowledge of the spatial spectrum of the input wave in order to avoid insufficient or, on the contrary, excessive damping of the second term in Eq. (13). Analysis of this problem is beyond the scope of this paper.

3.3. Validity limits

We now turn our attention to an assessment of the validity conditions for Eq. (5). As follows from the description of our test objects above, the condition $|\Delta\mu| \ll 1$ (see Sections 2.1 and 2.3) is satisfied for both objects. On the other hand, neither can be treated as weak objects as the maximum phase shifts of both objects are larger than one. Thus, we should check the validity conditions formulated in Section 2.3 (weakly absorbing object with slowly varying refractive index). In order that Eq. (5) be valid for free space propagation, the phase variations in the object plane on the length scale $\lambda z u_{\max}$ have to be small compared to unity (see Section 2.3). The value of the maximum spatial frequency $u_{\max}$ was found from the following considerations. It is worth mentioning that the finite resolution of the detector was taken into account in our numerical simulations (see Section 3.1). A Gaussian function with standard deviation of 10 pixels (43.9 μm) was used to simulate the PSF of the detector. As a result, the spatial spectrum of the images was limited to $u_{\max} \approx 0.01\ \mu\text{m}^{-1}$, resulting in $\lambda z u_{\max} \approx 1.24$ μm. Similarly, for Eq. (5) to be valid in the case of analyser-based imaging, the phase variations in the object plane should be small on the length scale $l_{\text{ext}}\gamma_0$ (see Section 2.3) which is approximately 1.524 μm for the chosen symmetrical Si (1 1 1)-reflection at wavelength 0.62 Å. The values of the maximum phase change corresponding to these two length scales are presented in Table 2. The values 0.365 and 0.410 rad (for PB and AB imaging, respectively) for object 1 are small enough to satisfy the validity conditions of Eq. (5) for free space propagation and diffraction in the analyser crystal. We should note, however, that in the case of 1.5″ deviation (which corresponds to the right edge of the crystal rocking curve) the reconstruction accuracy is worse compared to the case of 2.5″ deviation of the analyser (the latter corresponds to the right tail of the rocking curve). Comparison of the profiles presented in Figs. 4(c) and (d) shows that the difference in reconstruction of images collected at 1.5″ and 2.5″ is mainly due to the inaccuracy in reconstruction of the ABI phase contrast. The latter can be explained if we take into account the fact that in ABI, strictly speaking, the length scale, on which the phase should vary slowly in order that Eq. (5) be valid, depends on the deviation angle of the analyser [18]. This length scale is at its maximum at the edges of the rocking curve and decreases with angular deviation from these positions. In the case of object 2, the validity conditions for Eq. (5) are violated for both PBI and ABI contrast. The reconstruction accuracy is therefore much worse compared to that of object 1. However, as follows from the analysis of reconstructed phase cross sections in Fig. 6, the quality of PBI reconstruction

is very good. The origin of the large reconstruction error is in the ABI phase contrast. Again, the error of reconstruction is much worse in the case of 1.5″ deviation of the analyser while for 2.5″ deviation the reconstruction accuracy is quite satisfactory.

4. Partial coherence

So far we have assumed the input wave to be plane monochromatic and thus completely coherent. In real experiments the input wave is only partially coherent due to the polychromaticity and finite size of the source. This fact substantially complicates the calculation of intensity of the output wave as all quantities in Eq. (5) depend implicitly on the wavelength. Non-flatness of the input wavefront should also be taken into account. The shape of the latter is non-trivial and strongly depends on the source characteristics and optical elements which are usually present in the imaging system before the object. We restrict ourselves to only qualitative consideration of the coherence issues for the imaging setup presented schematically in Fig. 7 and consisting of a source (S), monochromator (M), test object (O), analyser (A) and detector (D). This configuration is typical for analyser-based phase-contrast imaging. We assume the source to be totally incoherent, i.e., radiation from different points of the source does not interfere and thus each point of the source forms an independent image in the detector plane. Let $S(x_0, y_0, \lambda)$ denote the spectral density of the source and $I_{\text{out}}(x, y; x_0, y_0, \lambda)$ be the intensity of the output wave produced by a monochromatic point source with wavelength λ and coordinates (x_0, y_0) in the source plane. Then the intensity of the output wave for a polychromatic finite source is written as follows:

$$I_{\text{out}}(x, y) = \int\int \mathrm{d}x_0\, \mathrm{d}y_0 \int \mathrm{d}\lambda S(x_0, y_0, \lambda) I_{\text{out}}(x, y; x_0, y_0, \lambda). \tag{15}$$

4.1. Effect of polychromaticity (temporal coherence)

In order to qualitatively characterise formation of an image according to Eq. (15), we performed the following numerical experiment. We used the experimental configuration shown in Fig. 7 with the following parameters:

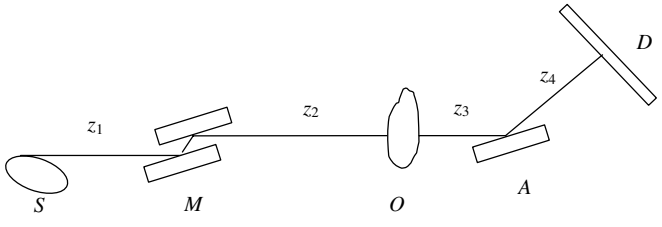

Fig. 7. Phase-contrast imaging setup used in the numerical simulations in the case of a point polychromatic X-ray source.

(a) Source: we considered a polychromatic point source located at position $(x_0, 0)$ in the source plane, the energy spectrum of which was taken to be uniform within the interval $[\lambda_0 - \Delta\lambda/2, \lambda_0 + \Delta\lambda/2]$ and zero outside, where $\lambda_0 = 0.62$ Å.
(b) Monochromator: we considered a symmetrical (1 1 1)-reflection for each of two semi-infinite silicon crystals positioned at the exact Bragg angle corresponding to the central wavelength λ_0.
(c) Object: we chose a water filled cylindrical hole of radius $r = 300$ μm in a polyethylene block with parallel surfaces; noting that for the chosen λ_0 the optical properties of the object are $\varphi_{\max} = -1.826$ rad, $\mu_{\max} = 0.01096$, $\delta/\beta = 166.9$.
(d) Analyser: we considered a single symmetrical (1 1 1)-reflection of a semi-infinite silicon crystal detuned at an angle $\omega = 1.5''$ from the exact Bragg position corresponding to the central wavelength λ_0.
(e) Propagation distances: $z_1 + z_2 = 40$ m, $z_3 + z_4 = 2$ m.

Fig. 8 shows calculated intensity profiles (in the directions orthogonal to the optical axis and parallel to the plane of diffraction of monochromator and analyser crystals) at the entrance plane of the object (a, b) and in the image plane (c, d). Each plot contains two profiles corresponding to different positions of the point source with respect to the optical axis. Intensity profiles presented in Figs. 8(a) and (c) were calculated for a monochromatic source ($\Delta\lambda = 0$) while those in Figs. 8(b) and (d) correspond to a polychromatic source ($\Delta\lambda/\lambda_0 = 10^{-3}$).

Analysis of Fig. 8 allows us to make several important conclusions regarding formation of the phase-contrast image in the configuration presented in Fig. 7. First, due to the high angular selectivity of the monochromator and analyser crystals, only a small part of the spherical wavefront from a point monochromatic source participates in formation of the image (see Figs. 8(a) and (c)). As the crystals have a strict relationship between the wavelength and the Bragg angle, at different wavelengths, different parts of the spherical wavefront give rise to the resultant image. We note that the image profile shown in Fig. 8(c) hardly resembles the expected one of the cylindrical object. This situation changes drastically if we calculate images formed by a point polychromatic source. In this case the intensity at the entrance plane of the object becomes uniform (see Fig. 8(b)) and the resultant intensity distribution in the detector plane (see Fig. 8(d)) is a familiar image of the cylinder, similar to that calculated using a plane monochromatic incident wave. The qualitative explanation of this behaviour is in the fact that intensity profiles, corresponding to the same point source but different wavelengths, are shifted along the x-axis with respect to each other. Integration of the image over the spectral density results in summation of all these profiles and, as a result, smearing of the interference fringes seen in Figs. 8(a) and (b). Meanwhile, positions of the intensity modulations in the detector plane, arising due to the object, are the same for all wave-

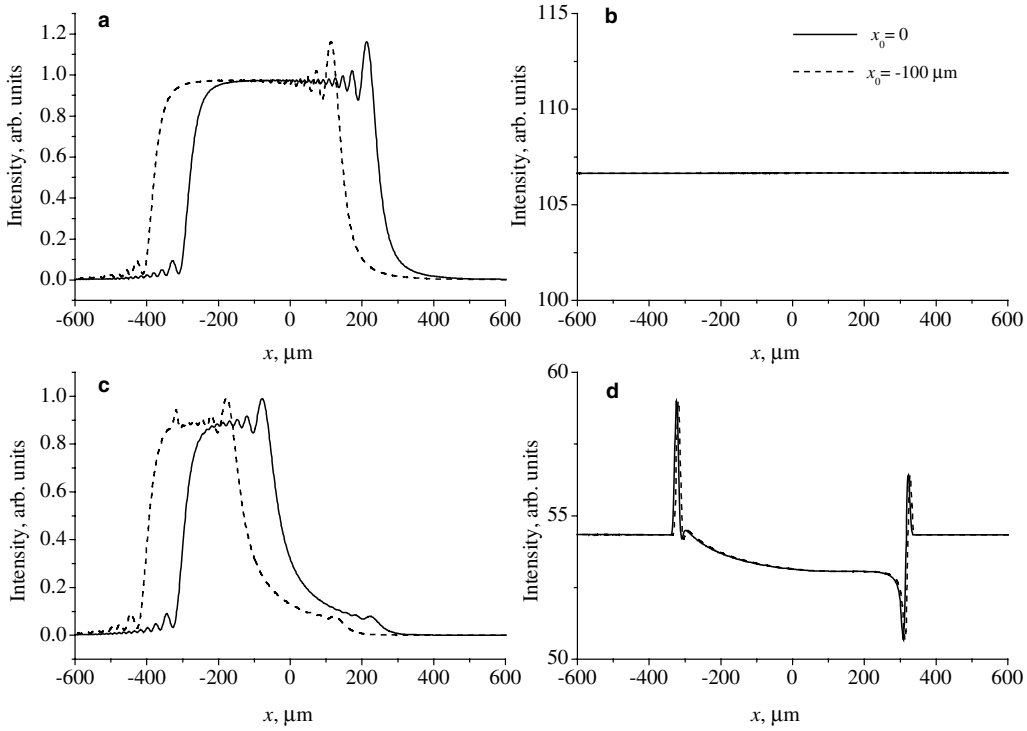

Fig. 8. Intensity cross-sections obtained by the numerical simulations for the phase-contrast imaging setup presented in Fig. 7. (a) The entrance plane of the object, monochromatic case; (b) the entrance plane of the object, polychromatic case; (c) the plane of the detector, monochromatic case; (d) the plane of the detector, polychromatic case. Solid lines – point source on the optical axis of the system; dashed lines – point source shifted by 100 μm down from the optical axis.

lengths. Summation of the intensity profiles corresponding to different wavelengths results in the appearance of the contrast in the intensity profile shown in Fig. 8(d). Thus, the first conclusion can be formulated as follows: *a small degree of polychromaticity in the source is not an obstacle for observing the AB phase-contrast image but, on the contrary, is necessary in order to observe it*.

4.2. Effect of finite source size (spatial coherence)

The second part of our discussion concerns the influence of the source size on the image formation. To this end, each plot in Fig. 8 presents two intensity profiles calculated for different point source positions. The solid profiles correspond to the point source at the optical axis of the imaging setup while the dashed profiles are obtained for a point source shifted by 100 μm from the optical axis. Comparison of these profiles in Fig. 8(a), corresponding to the entrance plane of the object, shows that a shift of the source results in a corresponding shift of the intensity profile by the same distance. A similar result is observed in the image plane where the image of the shifted point source is shifted by the same distance. More careful comparison of profiles in Fig. 8(c) allows one to observe an additional small peak in the profile obtained from the shifted source which corresponds to the edge of the cylinder. Turning our attention to the polychromatic case, it is clear from Fig. 8(b) that the intensity profiles for both non-shifted and shifted polychromatic point sources are identical in intensity value but different in spectral content. A shift of the point source results in the corresponding 'shift' of the wavelength band giving non-zero contribution into the intensity distribution in the exit plane of the monochromator. This can be more clearly understood from the following considerations. If we consider a fixed point on the surface of the monochromator then the X-ray from the transversely shifted point source will impinge upon the crystal at an angle different from that of the X-ray from the non-shifted point source. Therefore, if the exact diffraction condition for a non-shifted point source is fulfilled for a certain wavelength λ then the exact diffraction condition for a shifted point source will be fulfilled for a different wavelength. As can be seen from Fig. 8(d), if the point polychromatic source is shifted by 100 μm from the optical axis, the image intensity profile shifts in the 'opposite' direction by 5 μm, i.e. exactly by a $(M-1)$-times smaller distance, where the magnification $M = z_{SD}/z_{SO}$ is equal to the total source-to-detector distance z_{SD} divided by the source-to-object distance z_{SO}. For results presented in Fig. 8, $z_{SD} = 42$ m, $z_{SO} = 40$ m and so $M = 1.05$. Thus, we can formulate our second conclusion as follows: *each point of the polychromatic spatially incoherent source produces an independent image which is a shifted version of the image obtained with the polychromatic point source located on the optical axis*. If each point of the source has the same spectral distribution then the spectral density

function of the source can be factorized, $S(x_0, y_0, \lambda) = S'(x_0, y_0)S''(\lambda)$, and the intensity distribution in the image obtained with a finite incoherent source can be presented as a convolution of the image obtained with the polychromatic point source located on the optical axis with the rescaled intensity distribution function of the source

$$I_{\text{out}}(x, y) = \int\int \mathrm{d}x_0\, \mathrm{d}y_0 S'(-(M-1)x_0, -(M-1)y_0) \times I'_{\text{out}}(x - x_0, y - y_0; 0, 0), \quad (16)$$

where $I'_{\text{out}}(x, y; x_0, y_0) \equiv \int \mathrm{d}\lambda S''(\lambda) I_{\text{out}}(x, y; x_0, y_0, \lambda)$.

The detailed theoretical analysis of the image formation for the point polychromatic source is beyond the scope of this paper and is studied separately in a forthcoming paper.

5. Conclusion

Both propagation-based and analyser-based phase-contrast imaging systems may be unified into a single hybrid system which possesses certain strengths of each modality considered separately. We have linearized the unified PBI/ABI problem under the assumption of a "weak scatterer" and derived explicit analytical expressions for the corresponding transfer functions. We have also shown that, similarly to the case of PBI [28], the requirement for phase variations in the transmitted beam to be small can be replaced by the less restrictive requirement for the phase to change slowly over a characteristic distance that is determined by the parameters of the crystal reflection and free-space propagation. The obtained analytical expressions for the transfer functions can be used for quantitative analysis of the combined PBI/ABI image contrast. It can also be used to solve the inverse problem of reconstruction of the object-plane complex amplitude from collected image intensities. This inverse problem often has to be solved as a first step for quantitative analysis of the sample, i.e., the analysis of the distribution of its complex refractive index, e.g., by performing 3D computed tomography reconstruction in the PBI/ABI regime. The solution to the same inverse problem can also be used in order to improve the spatial resolution beyond the limit determined in the direct PBI/ABI regime by the width of the Fresnel diffraction fringes and the crystal extinction length. Of course, other resolution limiting factors, such as the finite detector resolution, incident beam divergence, X-ray energy spread, etc., have to be taken into account as well. These factors, which are relevant to realistic PBI/ABI experiments, will be analysed in more detail in future studies. In particular, the analytical expressions for the PBI/ABI transfer functions in the case of partially coherent incident radiation will be the subject of our immediate investigation. Finally, we presented a numerical example demonstrating a solution of an inverse imaging problem in the PBI/ABI regime using the obtained analytical expression for the transfer function. This example has shown that an accurate reconstruction of the spatial distribution of the projected thickness of a weak homogeneous sample can be achieved by applying the proposed formalism to a single PBI/ABI image.

References

[1] R. Fitzgerald, Phys. Today 53 (2000) 23.
[2] A. Momose, T. Takeda, Y. Itai, Rev. Sci. Instrum. 66 (1995) 1434.
[3] C. Raven, A. Snigirev, I. Snigireva, P. Spanne, A. Souvorov, V. Kohn, Appl. Phys. Lett. 69 (1996) 1826.
[4] F. Beckmann, U. Bonse, F. Busch, O. Gunnewig, J. Comput. Assist. Tomogr. 21 (1997) 539.
[5] P. Cloetens, W. Ludwig, J. Baruchel, D. Van Dyck, J. Van Landuyt, J.-P. Guigay, M. Schlenker, Appl. Phys. Lett. 75 (1999) 2912.
[6] F.A. Dilmanian, Z. Zhong, B. Ren, X.Y. Wu, L.D. Chapman, I. Orion, W.C. Thomlinson, Phys. Med. Biol. 45 (2000) 933.
[7] S.C. Mayo, T.J. Davis, T.E. Gureyev, P.R. Miller, D. Paganin, A. Pogany, A.W. Stevenson, S.W. Wilkins, Opt. Exp. 11 (2003) 2289.
[8] A. Bronnikov, J. Opt. Soc. Am. A 19 (2002) 472.
[9] A. Snigirev, I. Snigireva, V. Kohn, S. Kuznetsov, I. Schelokov, Rev. Sci. Instrum. 66 (1995) 5486.
[10] S.W. Wilkins, T.E. Gureyev, D. Gao, A. Pogany, A.W. Stevenson, Nature (London) 384 (1996) 335.
[11] P. Cloetens, R. Barrett, J. Baruchel, J.-P. Guigay, M. Schlenker, J. Phys. D 29 (1996) 133.
[12] E. Förster, K. Goetz, P. Zaumseil, Kris. Tech. 15 (1980) 937.
[13] V.N. Ingal, E.A. Beliaevskaya, J. Phys. D 28 (1995) 2314.
[14] T.J. Davis, D. Gao, T.E. Gureyev, A.W. Stevenson, S.W. Wilkins, Nature (London) 373 (1995) 595.
[15] D. Chapman, W. Thomlinson, R.E. Johnston, D. Washburn, E. Pisano, N. Gmür, Z. Zhong, R. Menk, F. Arfelli, D. Sayers, Phys. Med. Biol. 42 (1997) 2015.
[16] T.J. Davis, J. X-ray Sci. Tech. 6 (1996) 317.
[17] E. Pagot, S. Fiedler, P. Cloetens, A. Bravin, P. Coan, K. Fezzaa, J. Baruchel, J. Härtwig, Phys. Med. Biol. 50 (2005) 709.
[18] K.M. Pavlov, T.E. Gureyev, D. Paganin, Ya.I. Nesterets, M.J. Morgan, R.A. Lewis, J. Phys. D 37 (2004) 2746.
[19] P. Coan, E. Pagot, S. Fiedler, P. Cloetens, J. Baruchel, A. Bravin, J. Synchrotron Radiat. 12 (2005) 241.
[20] K.M. Pavlov, T.E. Gureyev, D. Paganin, Ya.I. Nesterets, M.J. Kitchen, K.K.W. Siu, J.E. Gillam, K. Uesugi, N. Yagi, M.J. Morgan, R.A. Lewis, Nucl. Instrum. Methods Phys. Res., A 548 (2005) 163.
[21] D.R. Luke, J.V. Burke, R.G. Lyon, SIAM Rev. 44 (2002) 169.
[22] J.M. Cowley, Diffraction Physics, third ed., Elsevier, Amsterdam, 1995.
[23] A. Pogany, D. Gao, S.W. Wilkins, Rev. Sci. Instrum. 68 (1997) 2774.
[24] Ya.I. Nesterets, T.E. Gureyev, D. Paganin, K.M. Pavlov, S.W. Wilkins, J. Phys. D 37 (2004) 1262.
[25] T.E. Gureyev, T.J. Davis, A. Pogany, S.C. Mayo, S.W. Wilkins, Appl. Opt. 43 (2004) 2418.
[26] D. Paganin, S.C. Mayo, T.E. Gureyev, P.R. Miller, S.W. Wilkins, J. Microsc. 206 (2002) 33.
[27] L.D. Turner, B.B. Dhal, J.P. Hayes, A.P. Mancuso, K.A. Nugent, D. Paterson, R.E. Scholten, C.Q. Tran, A.G. Peele, Opt. Exp. 12 (2004) 2960.
[28] J. Guigay, Optik 49 (1977) 121.
[29] T.E. Gureyev, A. Pogany, D.M. Paganin, S.W. Wilkins, Opt. Commun. 231 (2004) 53.